Superior Energy-Storage Capacitors with Simultaneously Giant Energy Density and Efficiency Using Nanodomain Engineered BiFeO₃-BaTiO₃-NaNbO₃ Lead-Free Bulk Ferroelectrics

He Qi, Aiwen Xie, Ao Tian, and Ruzhong Zuo*

Dielectric capacitors are receiving a great deal of attention for advanced pulsed power owing to their high power density and quick charge/discharge rate. However, the energy density is limited and the efficiency and the thermal stability are also not ideal, which has been a longstanding obstacle to developing desirable dielectric materials. These concerns have are addressed herein by fabricating nanodomain-engineered BiFeO₃-BaTiO₃-NaNbO₃ bulk ferroelectrics, integrating a high-spontaneous-polarization gene, wide band gaps, and a heterogeneous nanodomain structure, generating record-excellent comprehensive performance of giant energy-storage density $W_{rec} \approx 8.12$ J cm⁻³, high efficiency $\eta \approx 90\%$ and excellent thermal stability (±10%, −50 to 250 °C) and ultrafast discharge rate ($t_{0.9} < 100$ ns). Significantly enhanced dielectric breakdown strength of BiFeO₃-based solid solutions is mainly attributed to the substitution of NaNbO₃, which provides an increased band gap, refined grain size, and increased resistivity. The formation of nanoscale domains as evidenced by piezoresponse force microscopy and transmission electron microscopy enables nearly hysteresis-free polarization-field response and temperature-insensitive dielectric response. In comparison with antiferroelectric capacitors, the current work provides a new solution to successfully design next-generation pulsed power capacitors by fully utilizing relaxor ferroelectrics in energy-storage efficiency and thermal stability.

Because of high power density and extremely high charge-discharge speed, dielectric capacitors have received increasing attention in recent years.[1,2] The recoverable energy storage density (W_{rec}) of dielectric capacitors can be calculated by $w_{rec} = \int_{P_r}^{P_{max}} E\, dP$, where P, P_{max}, and P_r are the polarization value at an electric field (E), the saturated polarization, and the remanent polarization, respectively. Therefore, to obtain excellent energy-storage properties, both a large

($P_{max} - P_r$) value and a high dielectric breakdown strength (E_B) should be required. Even though some intrinsic dielectric breakdown mechanisms are closely correlated with the material component, the E_B value can still be improved by optimizing the preparation process, doping technology, and so on.[2–5] It is known that P_r can be easily modulated by changing phase structure,[6] improving dielectric relaxation behavior,[7–9] or introducing defect engineering.[10] Differently, P_{max} is mainly limited by the element species, namely, the P_{max} value is dominated by the gene of the selected material system.[11–13] Therefore, the composition system with intrinsically high spontaneous polarization (P_s) should be crucial for achieving excellent energy-storage performances. Among various types of dielectrics, antiferroelectric (AFE) materials have exhibited obvious advantages so far, thus achieving a continuous rise of recently reported W_{rec} values.[1,2,14] However, the hysteresis of the electric field induced phase transition in AFEs during charging and discharging is inherently responsible for inadequate energy efficiency (η), even for most relaxor AFEs[14,15] in which high energy density has to compromise seriously with the efficiency and even the thermal stability. Low η values mean more dissipated heat, thus easily causing the failure of the capacitor in service. Thereby, how to simultaneously achieve desirable W_{rec}, η, and thermal stability has been a critical issue to be solved in the future in energy-storage capacitors. By comparison, relaxor ferroelectric (FE) materials with nanodomains exhibit giant advantages in energy-storage efficiency.[16–24] However, W_{rec} values are usually restricted by either relatively limited E_B values mainly due to their high permittivity or insufficient P_{max} values primarily due to the P_s genes of the materials themselves. In fact, these shortcomings have been remedied to a certain degree by making relaxor FE films with obviously enhanced E_B because of the size effect.[20–22]

BiFeO₃ (BF)-based perovskite FE solid solutions were found to exhibit giant $P_s \approx 100$ μC cm⁻²,[12,13] which is much superior

Dr. H. Qi, Dr. A. W. Xie, Dr. A. Tian, Prof. R. Z. Zuo
Institute of Electro Ceramics & Devices
School of Materials Science and Engineering
Hefei University of Technology
Hefei 230009, P. R. China
E-mail: piezolab@hfut.edu.cn

**ADVANCED
SCIENCE NEWS**
www.advancedsciencenews.com

**ADVANCED
ENERGY
MATERIALS**
www.advenergymat.de

to that of $BaTiO_3$ (BT) and $(Na,K)NbO_3$-based solid solutions (<40 μC cm^{-2}) as well as other Bi-based perovskites such as $(Bi_{0.5}Na_{0.5})TiO_3$ (BNT) and $Bi(Mg_{0.5}Ti_{0.5})O_3$ (<50 μC cm^{-2}).[3–10] From this point of view, BF-based compositions should offer much bigger potentials for obtaining excellent energy-storage properties. So far, obviously enhanced energy-storage properties have been achieved in modified BF-based relaxor FE ceramics,[16,17,23,24] yet the obtained W_{rec} value is still <3.5 J cm^{-3} because the permissible electric field is not high enough, which is much lower than that of most well-studied lead-free perovskite ceramics, such as $NaNbO_3$ (NN)-, BNT-, BT-, and $AgNbO_3$-based ceramics.[1–3,7–9,14,18,19,25,26] The E_B value is one of the most important parameters for energy storage dielectrics as it is the upper limit of the applied voltage. Generally, it depends on internal factors (dielectric constant, band gap (E_g), density, defects, grain size, grain boundary, and so on) and external factors (sample area, sample thickness and electrode shape/size, temperature, humidity, type of voltage, test duration, and so on).[1–5,21,22,27–29] On the one hand, The BF-based compositions own a relatively low band gap E_g.[27,30] On the other hand, BF-based ceramics usually exhibit relatively large dielectric loss and high conductivity owing to the volatilization of Bi and the reduction of Fe^{3+} during sintering.[31] Significantly improved energy-storage density can be achieved in BF-based dielectric capacitors through improving the E_B value by introducing multivalent elements and liquid phases as sintering aids or through fabricating films.[4,16,17,21–24]

In this work, $(0.67-x)BF-0.33BT-xNN$ solid solutions were manufactured for the energy-storage capacitors, considering that BT has a stable phase structure and a high resistivity, and NN has a larger band gap E_g. At the same time, 0.1 wt% MnO_2 and 2 wt% $BaCu(B_2O_5)$ (BCB) were simultaneously added into BF-BT-NN ceramics in order to inhibit the $Fe^{3+} \rightarrow Fe^{2+}$ reaction and optimize the sintering behavior. The achievement of significantly enhanced E_B value (≈ 36 kV mm^{-1}) and obvious dielectric relaxation behavior leads to an ultrahigh W_{rec} of ≈ 8.12 J cm^{-3} and a large η of $\approx 90\%$ simultaneously in the $x = 0.1$ ceramic at room temperature, together with excellent temperature stability in a wide temperature range of -50 to 250 °C. The underlying mechanism for enhancing E_B values was analyzed in detail.

The temperature- and frequency-dependent dielectric permittivity (ε_r) of $(0.67-x)BF-0.33BT-xNN$ ceramics sintered at their optimum temperatures are shown in Figure S1, Supporting Information. It can be seen that the $x = 0$ sample exhibits a sharp dielectric peak with maximal permittivity (ε_m) at ≈ 450 °C. With increasing NN content, the temperature at the dielectric maxima (T_m) obviously decreases. In the meanwhile, the ε_m value rapidly decreases in addition to the increased phase-transition diffuseness. Interestingly, a nearly flat permittivity versus temperature curve at 1 kHz can be achieved in the proximity of room temperature for compositions with $0.1 \leq x \leq 0.15$, suggesting a low-temperature coefficient of permittivity. Owing to an inversely proportional relationship between ε_r and E_B, high energy-storage density can be generally obtained in dielectrics with medium ε_r.[1] Therefore, appropriate ε_r and its good thermal stability for compositions with high NN contents would be beneficial for the achievement of excellent energy-storage properties.[6–9,18,32]

The evolution of dielectric relaxation behavior usually accompanies the change of domain morphology. **Figure 1**a–d and Figure S2, Supporting Information show the contact-mode PFM and the corresponding surface morphology images of $(0.67-x)BF-0.33BT-xNN$ ceramics at room temperature respectively, in which PFM amplitude images give the strength of the piezoelectric response, while the contrast in phase image represents the polarization orientation. Long-range ordered FE domains with strong and clear contrasts can be observed in the $x = 0$ sample (Figure 1a). It can be found that the increase of NN content has made FE domains gradually become smaller and more irregular. No clear patterns for domain structures can be observed as $x \geq 0.1$, which should be due to the appearance of polar nanoregions (PNRs). The piezoresponse amplitude also gradually decreases with increasing NN content because of the interaction with local random fields.[33–36] The formation of PNRs well interprets the enhanced dielectric relaxation behavior shown in Figure S1, Supporting Information, which can also ensure the ability of rapid polarization response to an external electric field and generate a low frequency-dependent polarization response.[9,24]

Accompanying the transition from normal FE to relaxor FE, P-E loops become slimmer and slimmer with increasing NN content, as shown in Figure 1e. Particularly, the dielectric response of $0.1 \leq x \leq 0.15$ compositions becomes insensitive to the external electric field, as clearly reflected by nearly linear hysteresis-free P-E loops. Both P_{max} and P_r exhibit an obvious decline with increasing x, and especially P_r decreases close to zero at $x \geq 0.08$. The ΔP ($= P_{max} - P_r$) value (≈ 20 μC cm^{-2}) was maximized at $x = 0.04$, resulting in the highest W_{rec} value (0.52 J cm^{-3}), as shown in Figure 1f. However, the $x = 0.04$ ceramic exhibits a relatively low η value (50%), meaning the dissipation of a large portion of the charged electric energy as heat during discharging. A good balance between W_{rec} and η has to be reached for industrial applications. By comparison, the $x = 0.1$ composition has a W_{rec} of 0.37 J cm^{-3} and a high η of 94% under 7 kV mm^{-1}. The reduced joule heat arising from hysteretic energy dissipation would retard the thermal breakdown for compositions with linear P-E loops. However, the W_{rec} value keeps a clear decreasing tendency with further increasing x up to 0.15, but the η value only slightly increases. This is also the reason why the $x = 0.1$ sample was chosen for further study. Although the W_{rec} value of the $x = 0.1$ ceramic under 7 kV mm^{-1} is still inferior to that of other reported ceramic dielectrics (see Figure 1g),[7–9,15–19,23–26,37,38] larger potentials can be expected if the applied electric field can be further increased.

The P-E loops measured at room temperature under different electric fields for the $x = 0.1$ ceramic are shown in **Figure 2**a. A low-hysteresis double-like P-E loop, instead of a purely linear dielectric response (non-FE state) or a centrosymmetric parabolic curve (nonergodic relaxor state), can be observed under an applied bipolar electric field of 36 kV mm^{-1}, demonstrating a typical characteristic of ergodic relaxor FE ceramics in the vicinity of the ergodic-nonergodic phase transition line.[39,40] This can be further accounted for by looking at its dP/dE ($=\varepsilon$) curve in Figure 2a, where there are two broad but overlapped humps during loading and unloading. The electric field-driven relaxor to FE phase transition leads to a continuously increased P_{max} value. The high local random field brings about a low-hysteresis dielectric response, a nearly zero P_r, and an extremely high driving field for the growth of PNRs and subsequent
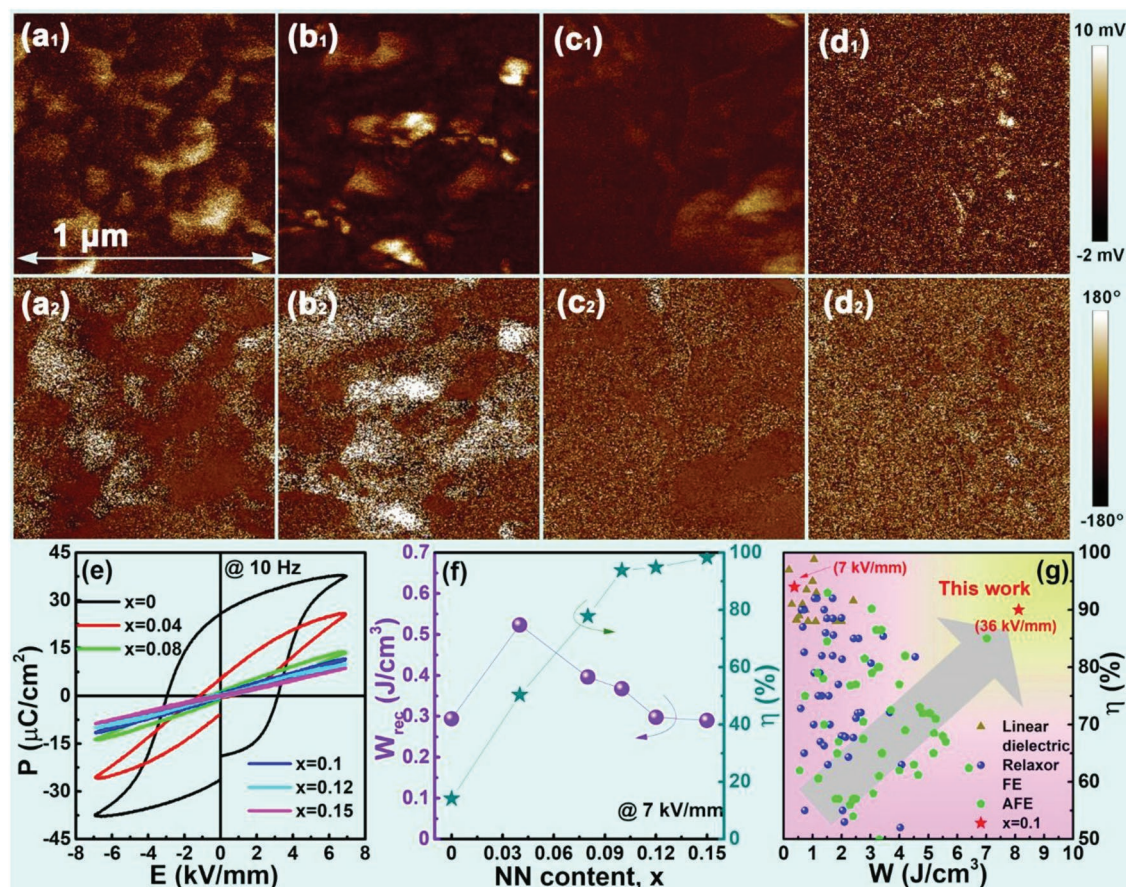
Figure 1. Out-of-plane PFM amplitude (subscript 1) and phase (subscript 2) images of $(0.67 - x)$BF-0.33BT-xNN ceramics: a) $x = 0$, b) $x = 0.04$, c) $x = 0.10$, and d) $x = 0.15$; e) Room-temperature P-E loops, f) W_{rec} and η values measured under 7 kV mm^{-1} for $(0.67 - x)$BF-0.33BT-xNN ceramics; g) a comparison of W_{rec} and η values among recently reported bulk ceramics.

orientation in response to the external electric fields.[33–36] As a result, an ultra-high η of over 90% was achieved in the studied electric field range, as shown in Figure 2b. Moreover, the W_{rec} value exhibits a nearly parabolic increase with loading electric field, up to a large W_{rec} of ≈8.12 J cm^{-3} under 36 kV mm^{-1}. As shown in Figure 1g, there seems to be an obvious compromising relation between W_{rec} and η for most of the reported energy-storage dielectrics. W_{rec} values in relaxor FEs and purely linear nonpolar dielectrics are usually restricted by limited P_{max} values under high fields owing to low E_B value and low ε_r value, respectively. AFE ceramics usually exhibit relatively good energy-storage properties owing to high P_{max}, particularly for relaxor AFEs showing even better energy-storage performances.[9,14,15,41] However, it is particularly worthy of note in current work that superior comprehensive properties through excellent balance between W_{rec} (≈8.12 J cm^{-3}) and η (>90%) values have been realized in BF-based relaxor FEs with $x = 0.1$ owing to inherently high P_s, high applied field, and fast polarization response, showing huge advantages for the application in pulsed power electronics. Compared with relaxor AFEs, which show obvious advantages in the aspect of W_{rec} (≈7.02 and ≈12.2 J cm^{-3} in BNT- and NN-based relaxor AFEs, respectively),[9,14] BF-based relaxor FEs prove to show obviously large advantages in energy-storage efficiency (≈85% and ≈69% in

BNT- and NN-based relaxor AFEs, respectively), as long as limited E_B can be effectively improved.

In order to reveal the actual charging-discharging performance, overdamped pulsed discharge electric current-time (I–t) curves as a function of electric field for the $x = 0.1$ ceramic are shown in Figure S3, Supporting Information. The discharge energy density (W_D) can be calculated by $W_D = R \int I(t)^2 \, dt / V$, where R and V are total load resistor (200 Ω) and the sample volume, respectively. It is clear that the current peak (I_{max}) increases linearly and W_D exhibits a parabolic increase with increasing electric field. According to the W_D-t curves measured under different electric fields in Figure 2c, it is clear that the $x = 0.1$ ceramic exhibits a fast discharging speed under 20 kV mm^{-1} with a short discharge time of $t_{0.9}$ ≈97 ns (Figure S3b, Supporting Information), which describes the discharge time corresponding to the 90% saturated W_D value. The $t_{0.9}$ value achieved in the $x = 0.1$ ceramic is much smaller than that of most reported relaxor FEs, AFEs, and polymer nanocomposite capacitors (usually on the level of hundreds of nanoseconds),[19,37,38,42] as can be clearly seen in Table S2, Supporting Information. This fast discharging speed should be ascribed to a nearly linear and hysteresis-free polarization response mainly from the ionic displacement (see Figure 1e). Therefore, accompanying the fast decrease of polarization, the stored energy during charging
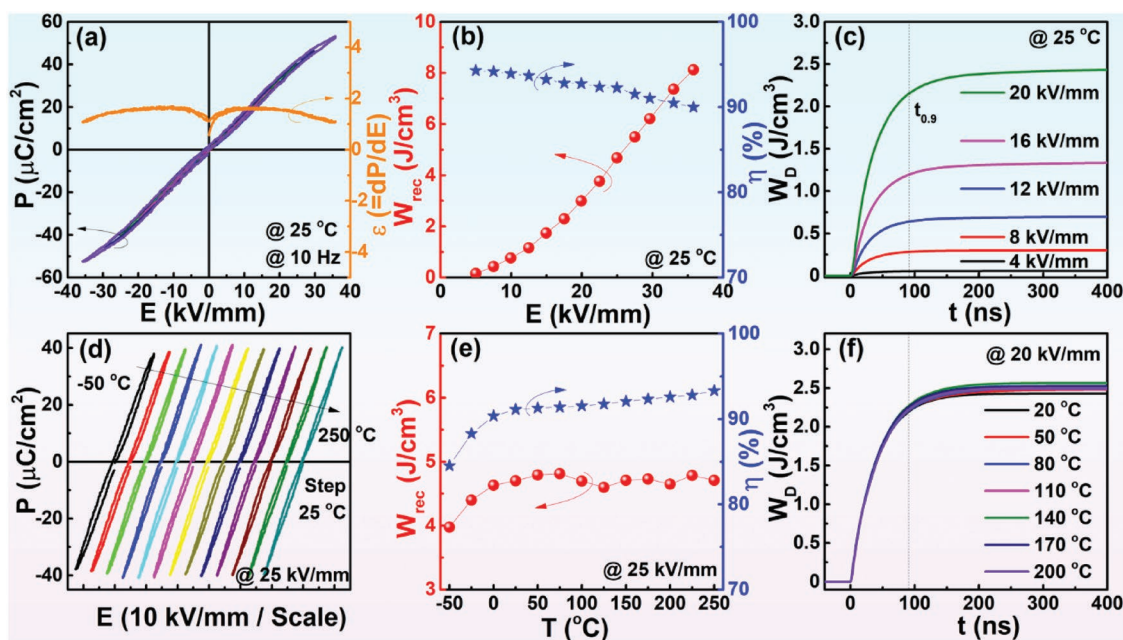
Figure 2. a) Room-temperature P-E loops and dP/dE measured under different electric fields for the $x = 0.1$ ceramic, and b) W_{rec} and η values and c) pulsed overdamped discharging W_D of the $x = 0.1$ ceramic with varying the magnitude of the applied electric field; d) P-E loops, e) corresponding W_{rec} and η values, and f) pulsed overdamped discharging W_D measured at various temperatures for the $x = 0.1$ ceramic.

can be released in a short time after the removal of the external electric field.

Considering that the $x = 0.1$ sample owns a linear-like polarization-field response, its energy-storage density W_{rec} can be estimated by using the equation: $W_{rec} = \varepsilon_0 \cdot \varepsilon_r \cdot E^2/2$. Therefore, temperature-stable dielectric response would benefit to the achievement of good thermal stability for energy-storage properties. Figure 2d shows P-E loops of the $x = 0.1$ ceramic under 25 kV mm^{-1} in the temperature range of −50 to 250 °C. The polarization hysteresis can be found to slightly decrease with increasing measuring temperature because the increased random electric field tends to enhance the response speed of PNRs to electric fields. At the same time, the achievable P_{max} value at 25 kV mm^{-1} changes very little with changing temperature. As a result, both W_{rec} and η increase on heating, as shown in Figure 2e. A large W_{rec} of 3.98–4.81 J cm^{-3} as well as a large η of >85% can be obtained in the temperature range of −50 to 250 °C in the studied composition. A detailed comparison was made in Figure S4, Supporting Information with some other recently reported dielectric ceramics,[9,14,16,26,38] demonstrating obvious advantages in the thermal stability of the $x = 0.1$ sample. Moreover, no evident change in I_{max} and I–t curves can be seen in the temperature range from room temperature to 200 °C, as shown in Figure S3, Supporting Information and Figure 2f, resulting in a temperature-insensitive W_D of ≈2.5 J cm^{-3} under 20 kV mm^{-1} in Figure 2f. A gradual decrease of $t_{0.9}$ can be achieved upon heating owing to the increased polarization response of PNRs to the external electric field.

Figure S5, Supporting Information shows the grain morphology of several selected (0.67-x)BF-0.33BT-xNN ceramics sintered at their optimum temperatures. It can be seen that all the samples have well-developed and uniform grains with a high relative density of >97%. With the substitution of NN

for BF, the average grain size (G_a) of the sintered ceramic was found to decrease from ≈1.05 µm at $x = 0$ to ≈0.58 µm at $x = 0.15$, as shown in **Figure 3**a, probably because of slightly decreased sintering temperature caused by the activation of lattices (high energy induced by the lattice distortion) in the solid solution.[43,44] The reduction of grain size should contribute to the enhancement of dielectric breakdown strength E_B as described by an exponential decay relationship with grain size, i.e., $E_B \propto (G_a)^{-a}$.[5] This is because the depletion space charge layers building up at grain boundaries tend to increase with increasing grain boundary fraction, which provides higher potential barriers for the charge carriers.[45]

The UV–vis absorption spectrum is known to be relevant to the electronic structure feature and the energy band of semiconductor catalysts. As shown in Figure S6, Supporting Information and Figure 3a, the E_g values can be calculated by using the plot of $(\alpha h v)^2$ versus photon energy hv, where α is absorbance coefficient, h the Planck constant, and v the frequency. Pure NN exhibits a large E_g of ≈3.58 eV. Accordingly, the introduction of NN into BF-BT was found to cause a monotonous increase of E_g. Accompanying the increase of E_g, the electrons in the valence band get harder to jump into the conduction band, which should lead to the decreased conductivity and thus low possibility of intrinsic breakdown.[1,27]

The conduction mechanism and dielectric relaxation induced by defects can be commonly analyzed by the measurement of complex impedance (Z^*), in which Z' and Z'' are the real and imaginary parts of impedance, respectively. All the studied curves measured at 400 °C in Figure S7a, Supporting Information shows a nearly single *Debye* semicircle arc, indicating the introduction of NN into BF-BT can significantly enhance the resistivity of materials. According to the fitting results shown in Figure S7b, Supporting Information by using the $x = 0.1$
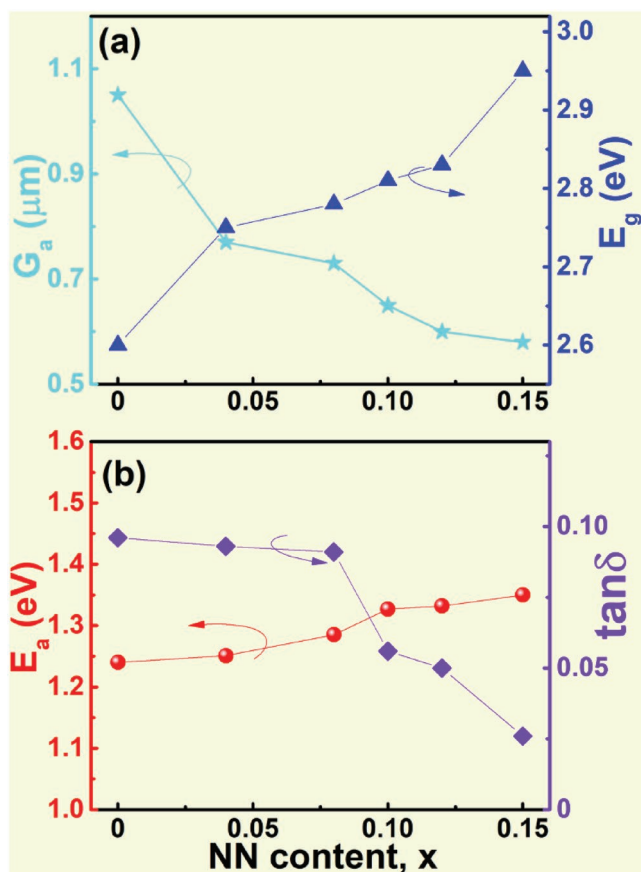
Figure 3. The variation of a) average grain size G_a, band gap E_g; b) E_a of grain boundary and room-temperature $tan\delta$ at 1 MHz with changing NN content.

ceramic as an example, it is evident that the conduction mechanism should be dominated by a grain boundary. As a result, the increased fraction of grain boundary with increasing NN content (Figure 3a and Figure S5, Supporting Information) would be in favor of the enhanced resistivity. Figure S7c, Supporting Information shows the Z''/Z''_{max} value as a function of frequency for the $x = 0.1$ ceramic in the temperature of 300–600 °C. Only one peak can be observed, which shifts towards higher frequency with increasing temperature. The activation energy (E_a) associated with the potential-energy barrier can be estimated by the *Arrhenius* law $\sigma = \sigma_0 exp(E_a/kT)$,[46] where σ is the bulk conductivity, σ_0 is the pre-exponent constant and k is the *Boltzmann* constant. As calculated from the slope of $ln\sigma$-$1000/T$ plots in Figure S7d, the E_a value of grain boundary and grain in the range of 1.24–1.35 eV (Figure 3b) and 1.19–1.33 eV, respectively, suggests a main conduction mechanism from oxygen vacancies in both grain boundaries and grains. The formation of oxygen vacancies can be believed to correlate with the reduction of Fe^{3+} and the volatility of Bi^{3+} during sintering, both of which can be effectively restricted by the addition of 0.1 $wt.\%$ MnO_2 as electron trapper and 2 wt% BCB as sintering aid, respectively, apart from the substitution of NN for BF. In a word, the increased total resistivity of the sample with increasing x should be in favor of enhancing E_B and decreasing dielectric loss (Figure 3b).

Nevertheless, the E_B value can be practically evaluated by the "Weibull" distribution function based on the statistical nature of failure using a linear relationship between $ln\{ln[1/(1-i/(n+1))]\}$ and $ln(E_i)$,[47] where n is the total number of the samples and E_i is the breakdown electric field for the ith specimen arranging in the ascending order. As shown in **Figure 4**, all data points fit well with the *Weibull* distribution with a slope (the "Weibull" modulus m) of more than five for all the studied compositions, demonstrating high reliability of the "Weibull" analysis. According to the linear regression of the $ln\{ln[1/(1-i/(n+1))]\}$ versus lnE relation, the *Weibull* moduli E_B value can be determined. The average E_B was found to increase monotonously from 23 to 42 kV mm^{-1} with increasing NN content from $x = 0$ to $x = 0.15$. The increased E_B provides a solid fundament for achieving good energy storage properties in $(0.67 - x)$ BF-0.33BT-xNN ceramics with high NN content, which should be basically related to the optimization of both intrinsic and extrinsic breakdown mechanisms.

In order to achieve a deep understanding of the structural nature for achieving excellent energy storage properties, TEM analysis was performed for the $x = 0.1$ sample, as shown in **Figure 5**. According to the HR-TEM image of lattice fringes and the SAED patterns in Figure 5a–d, the studied sample exhibits a good crystalline quality. Moreover, typical $1/2\{ooo\}$ superlattice reflection (o and e stand for the odd and even Miller indices, respectively)[48] can be observed along $[110]_C$ direction, suggesting an $R3c$ local symmetry inheriting from the matrix BF. Complex domain patterns, which are composed of randomly distributed PNRs in the matrix with weak contrasts, were observed, as shown in Figure 5e. As locally magnified in Figure 5f, typical stripe-like PNRs with a width of ≈ 3 nm are comparable with those observed in $Pb(Mg_{1/3}Nb_{2/3})O_3$-based ergodic relaxor FEs.[40] Although the appearance of moiré fringes in ferroelectrics is also related to the existence
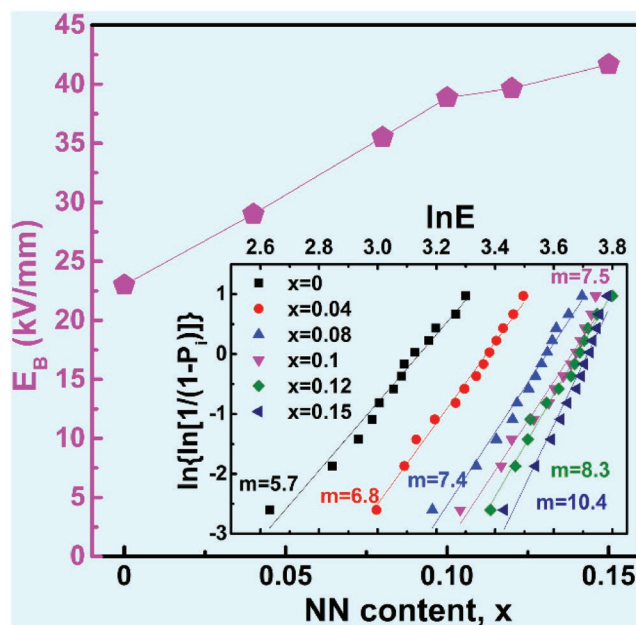
Figure 4. "Weibull" distribution and calculated E_B values of $(0.67 - x)$ BF-0.33BT-xNN ceramics.

ADVANCED
SCIENCE NEWS
www.advancedsciencenews.com

ADVANCED
ENERGY
MATERIALS
www.advenergymat.de
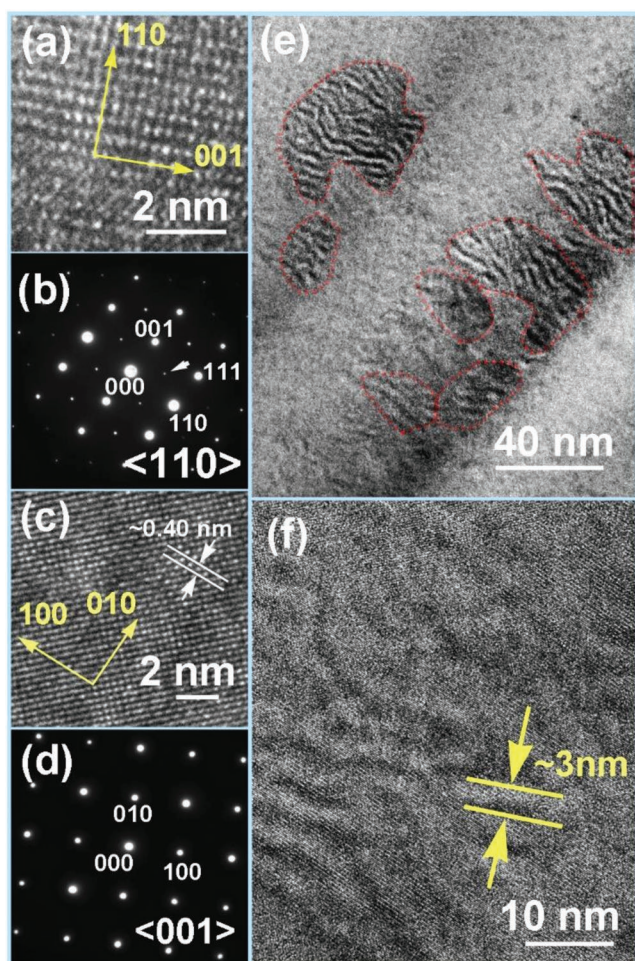
Figure 5. a) HR-TEM images of lattice fringes and b) SAED patterns along $[110]_c$; c) HR-TEM images of lattice fringes, d) SAED patterns, and e and f) domain morphology on different scales along $[001]_c$ for the $x = 0.1$ ceramic at room temperature.

of short-range ordering, yet they are usually periodic parallel stripes, and superlattice diffraction dots might be observed at the same time. However, none of these features can be found in Figure 5. Even though the locally ordered arrangement of atoms can be observed from HR-TEM images, the appearance of randomly distributed PNRs still indicates the existence of local chemical heterogeneity,[33,36,39,40] owing to the increased ionic disorder on the equivalent lattice sites after the introduction of NN into BF-BT.[36] The formation of compositional heterogeneity might be related to the big difference among the respective optimum sintering temperatures of the constituents: BF, BT, and NN compounds, leading to the large difference of their sintering activities during sintering of the studied sample. The BF-rich regions can be formed first due to the higher reactivity of the constituent oxides, while the BT and NN-rich regions are incorporated at later stages of sintering. This formation mechanism was supported in BF–BT binary ceramics in which BF-rich cores and BT-rich shells were observed by TEM.[49] Besides, the addition of MnO_2 and BCB shows an effect of retarding grain growth and interferes with the chemical homogenization during sintering. As known, BF exhibits a

large lattice distortion owing to both Bi 6s-O 2p and Fe 3d-O 2p orbital hybridization,[50,51] yet Na and Ba exhibit a strong ionic character, showing little contribution to the polarization owing to lack of orbital hybridization. As a result, relatively large PNRs can be formed at the BF-rich regions. At BT- and NN-rich regions, short-range ordering regions are indistinguishable due to much smaller scales. In a word, the compositional inhomogeneity was found to result in the structure heterogeneity including the formation of PNRs in the $x = 0.1$ ceramic, leading to a rapid polarization response to the external electric field.

An important indication of the structure heterogeneity is the enhanced temperature stability of dielectric properties.[18,32,52] Rietveld refinements of XRD patterns at different temperatures for the $x = 0.1$ ceramic are shown in **Figure 6**a–e. The refined structure parameters and various agreement factors are listed in Table S1, Supporting Information. Even though a local $R3c$ symmetry can be identified by SAED patterns in Figure 5, the fitting results of XRD patterns indicate that the $Pm\overline{3}m$ (cubic phase) model shows a better agreement between the observed and calculated profiles with reliability factors of weighted patterns (R_{wp}), patterns (R_p), and the goodness-of-fit indicator (χ^2) in the range of 5.87–5.94%, 4.55–4.73%, and 1.14–1.16%, respectively. The large difference between local and average structures should be ascribed to the fact that the PNRs are so small that their inherent $R3c$ symmetry can hardly be resolved by X-ray. The identification of an average cubic phase in the studied temperature range indicates the existence of PNRs even at −50 °C. Temperature-dependent Raman spectra are shown in Figure 6f, which can reflect the change in local structure. Three relatively strong scattering peaks A_{1g} ($v1$), F_{2g} ($v5$), and F_{2u} ($v6$) can be detected, which are assigned to the NbO_6 octahedron stretching, bending, and bending vibration modes, respectively. Although both an obvious increase of the full width at half maximum and an obvious decrease of the peak intensity for these modes can be observed with increasing temperature, local noncubic clusters still exist till 250 °C. This should be ascribed to the fact that all atoms in the cubic $Pm\overline{3}m$ phase are located at sites having a center of inversion and therefore all Raman active modes are forbidden. The position of all Raman peaks shifts to lower wavenumber upon heating, indicating the weakening of B-O bonds. Therefore, the existence of PNRs within a wide temperature range would ensure linear-like polarization response up to 250 °C, which is responsible for temperature-insensitive energy storage properties.

In summary, the (0.67-x)BF-0.33BT-xNN ternary lead-free FE ceramics have been prepared via a solid-state reaction method. The substitution of NN for BF was surprisingly found to provide a couple of merits including increased band gaps, decreased grain size, and enhanced resistivity, which are all together responsible for the significant improvement of dielectric breakdown strength. Moreover, an obvious structure heterogeneity particularly for compositions with higher NN contents results in a nearly hysteresis-free polarization response to the external electric field and a temperature-insensitive large dielectric response. As a consequence, a giant W_{rec} ≈8.12 J cm^{-3} and a high η ≈90% as well as an outstanding charge–discharge performance ($t_{0.9}$ ≈100 ns) were achieved simultaneously in the $x = 0.1$ bulk ceramic at room temperature. Furthermore, desirable W_{rec} (≈4.40 ± 0.44 J cm^{-3}) and η (>85%) can be also
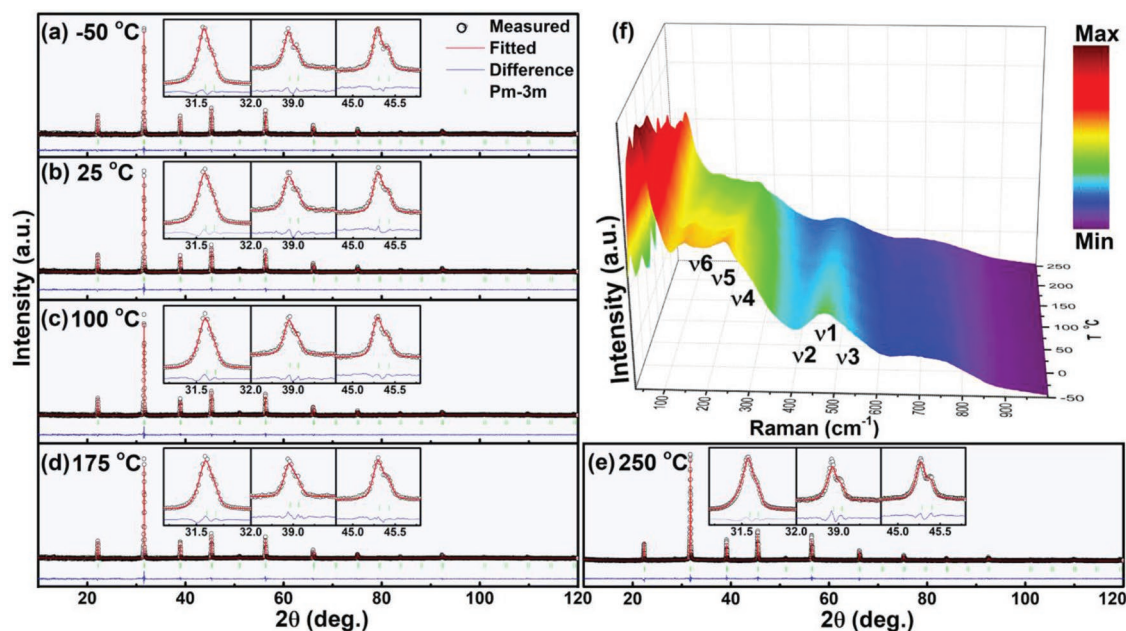
Figure 6. The Rietveld refinement results of XRD patterns for the $x = 0.1$ ceramic measured at various temperatures: a) −50, b) 25, c) 100, d) 175, and e) 250 °C; f) Raman spectra of the $x = 0.1$ ceramic measured at various temperatures. The insets of (a)–(e) show the enlarged *(110)*, *(111)*, and *(200)* diffraction lines at the corresponding temperatures.

obtained in a wide temperature range of −50 to 250 °C. These results demonstrate that the BF–BT–NN relaxor FE solid-solution ceramics can be considered as potential lead-free dielectrics for next-generation pulsed power capacitors.

Experimental Section

Material Synthesis: The $(0.67\text{-}x)BF\text{-}0.33BT\text{-}xNN$ $(0 \leq x \leq 0.15)$ ceramics were fabricated by a conventional solid-state reaction method. Bi_2O_3 ($\geq 99.0\%$), Fe_2O_3 ($\geq 99.0\%$), $BaCO_3$ ($\geq 99.0\%$), TiO_2 ($\geq 99.0\%$), Na_2CO_3 ($\geq 99.0\%$), and Nb_2O_5 ($\geq 99.0\%$) (Sinopharm Chemical Reagent Co., Ltd., CN) were used as the starting materials. The stoichiometric powder was first synthesized through calcination at 700–800 °C. Afterward, 0.1 wt% MnO_2 and 2 wt% BCB powder were mixed with the as-synthesized powder through ball milling together with 0.5 wt% PVB binder. The sample discs were sintered at 920–980 °C in a sacrificial powder of the same composition in closed crucibles. For measuring electrical properties, the ceramic discs were polished into a thickness of ≈0.15 mm and then two parallel surfaces were covered with silver paste, and finally fired at 550 °C for 30 min as electrodes.

Dielectric Measurements: Dielectric properties as a function of temperature and frequency were measured by an LCR meter (Agilent E4980A, Santa Clara, CA) at a heating rate of 180 °C h^{-1}.

Piezoresponse Force Microscopy: The piezoresponse force microscopy (PFM) mode of an atomic force microscope (NanoManTM VS, Vecco, USA) was used to analyze the domain structure. Before PFM observation, the disk samples were polished into a thickness of ≈0.1 mm and then thermally etched at 850 °C for 30 min.

Ferroelectric Measurements: The temperature-dependent *P–E* hysteresis loops were measured using an FE test system (Precision Multiferroelectric; Radiant Technologies Inc, Albuquerque, New Mexico) connected with a high-temperature probing stage (HFS600E-PB2, Linkam Scientific Instruments, Tadworth, UK).

Energy Storage Properties: The energy release properties of ceramic capacitors were investigated by a commercial charge-discharge platform (CFD-001, Gogo Instruments Technology, Shanghai, China) with a

certain discharge resistance, inductance, and capacitance (RLC) load circuit. For the pulsed charge–discharge test, the sample size is 0.2 mm (thickness) × 4.9 mm^2 (electrode area).

Scanning Electron Microscopy: The grain morphology of the samples was observed using a field-emission scanning electron microscope (FE-SEM; SU8020, JEOL, Tokyo, Japan). Before SEM observation, the disk samples were polished and then thermally etched at 850 °C for 30 min.

Impedance Test: A precision impedance analyzer (4294A, Agilent Technologies, Santa Clara, CA, USA) was used to measure the temperature-dependent impedance spectra in the frequency range of 20 Hz to 1 MHz.

Optical Absorption: The optical absorption properties of the particle samples were measured in the range of 200–1500 nm using a UV-vis spectrophotometer (TU-1950, Beijing Perkinje General Instrument Co., Ltd, Beijing, China) with an integrating sphere.

Dielectric Breakdown Test: The E_B measurement was performed at room temperature by using a voltage-withstand test device (BDJC-50KV, Beiguangjingyi Instrument Equipment Co. Ltd., Beijing, China) with the sample size of about 0.15 mm (thickness) × 4.9 mm^2 (electrode area).

Transmission Electron Microscopy: The domain morphology observation, selected area electron diffraction (SAED), and high-resolution (HR) atomic imaging were performed on a field-emission transmission electron microscope (TEM, JEM-2100F, JEOL, Japan) operated at 200 kV. Before TEM examination, samples were mechanically polished to a thickness of ≈20 μm and then ion-milled on a Precision Ion Polishing System (PIPS, Model 691, Gatan Inc., Pleasanton, CA, USA) at ≈5 kV. All specimens were annealed at 80 °C for at least 1 day to release the mechanical stress before the TEM measurement.

Temperature-Dependent X-Ray Diffraction: X-ray diffraction (XRD) measurements under different temperatures were performed using a powder diffractometer with Cu $K\alpha$ radiation under an acceleration condition of 40 kV and 30 mA (D/Max2500V; Rigaku, Tokyo, Japan). Rietveld structure refinements were performed by using the program *GSAS*.

Raman Spectra: Temperature-dependent Raman spectra were collected on well-polished pellets by 532 nm excitation using a Raman spectrometer (LabRam HR Evolution, HORIBA JOBIN YVON, Longjumeau Cedex, France).

Conflict of Interest

The authors declare no conflict of interest.

[1] L. T. Yang, X. Kong, F. Li, H. Hao, Z. X. Cheng, H. X. Liu, J. F. Li, S. J. Zhang, *Prog. Mater. Sci.* **2019**, *102*, 72.

[2] A. Chauhan, S. Patel, R. Vaish, C. R. Bowen, *Materials* **2015**, *8*, 8009.

[3] Y. H. Huang, Y. J. Wu, W. J. Qiu, J. Li, X. M. Chen, *J. Eur. Ceram. Soc.* **2015**, *35*, 1469.

[4] G. Wang, J. L. Li, X. Zhang, Z. M. Fan, F. Yang, A. Feteira, D. Zhou, D. C. Sinclair, T. Ma, X. L. Tan, D. W. Wang, I. M. Reaney, *Energy Environ. Sci.* **2019**, *12*, 582.

[5] T. Tunkasiri, G. Rujijanagul, *J. Mater. Sci. Lett.* **1996**, *15*, 1767.

[6] L. L. Fan, J. Chen, H. J. Kang, L. J. Liu, L. Fang, J. X. Deng, R. B. Yu, X. R. Xing, *J. Appl. Phys.* **2012**, *111*, 104118.

[7] J. Y. Wu, A. Mahajan, L. Riekehr, H. F. Zhang, B. Yang, N. Meng, Z. Zhang, H. X. Yan, *Nano Energy* **2018**, *50*, 723.

[8] T. Q. Shao, H. L. Du, H. Ma, S. B. Qu, J. Wang, J. F. Wang, X. Y. Wei, Z. Xu, *J. Mater. Chem. A* **2017**, *5*, 554.

[9] H. Qi, R. Z. Zuo, *J. Mater. Chem. A* **2019**, *7*, 3971.

[10] X. B. Ren, *Nat. Mater.* **2004**, *3*, 91.

[11] R. E. Cohen, *Nature* **1992**, *358*, 136.

[12] J. B. Neaton, C. Ederer, U. V. Waghmare, N. A. Spaldin, K. M. Rabe, *Phys. Rev. B* **2005**, *71*, 014113.

[13] D. Lebeugle, D. Colson, A. Forget, M. Viret, *Appl. Phys. Lett.* **2007**, *91*, 022907.

[14] H. Qi, R. Z. Zuo, A. W. Xie, A. Tian, J. Fu, Y. Zhang, S. J. Zhang, *Adv. Funct. Mater.* **2019**, *29*, 1903877.

[15] P. Mohapatra, Z. M. Fan, J. Cui, X. L. Tan, *J. Eur. Ceram. Soc.* **2019**, *39*, 4735.

[16] N. T. Liu, R. H. Liang, Z. Y. Zhou, X. L. Dong, *J. Mater. Chem. C* **2018**, *6*, 10211.

[17] D. W. Wang, Z. M. Fan, D. Zhou, A. Khesro, S. Murakami, A. Feteira, Q. L. Zhao, X. L. Tan, I. M. Reaney, *J. Mater. Chem. A* **2018**, *6*, 4133.

[18] Q. B. Yuan, G. Li, F. Z. Yao, S. D. Cheng, Y. F. Wang, R. Ma, S. B. Mi, M. Gu, K. Wang, J. F. Li, H. Wang, *Nano Energy* **2018**, *52*, 203.

[19] M. X. Zhou, R. H. Liang, Z. Y. Zhou, X. L. Dong, *J. Mater. Chem. C* **2018**, *6*, 8528.

[20] N. N. Sun, Y. Li, Q. W. Zhang, X. H. Hao, *J. Mater. Chem. C* **2018**, *6*, 10693.

[21] H. Pan, J. Ma, J. Ma, Q. H. Zhang, X. Z. Liu, B. Guan, L. Gu, X. Zhang, Y.-J. Zhang, L. L. Li, Y. Shen, Y.-H. Lin, C.-W. Nan, *Nat. Commun.* **2018**, *9*, 1813.

[22] H. Pan, F. Li, Y. Liu, Q. H. Zhang, M. Wang, S. Lan, Y. P. Zheng, J. Ma, L. Gu, Y. Shen, P. Yu, S. J. Zhang, L.-Q. Chen, Y.-H. Lin, C.-W. Nan, *Science* **2019**, *365*, 578.

[23] D. G. Zheng, R. Z. Zuo, D. S. Zhang, Y. Li, *J. Am. Ceram. Soc.* **2015**, *98*, 2692.

[24] D. G. Zheng, R. Z. Zuo, *J. Eur. Ceram. Soc.* **2017**, *37*, 413.

[25] Y. Tian, L. Jin, H. F. Zhang, Z. Xu, X. Y. Wei, E. D. Politova, S. Y. Stefanovich, N. V. Tarakina, I. Abrahams, H. X. Yan, *J. Mater. Chem. A* **2016**, *4*, 17279.

[26] L. Zhao, Q. Liu, J. Gao, S. J. Zhang, J. F. Li, *Adv. Mater.* **2017**, *29*, 1701824.

[27] C. Kim, G. Pilania, R. Ramprasad, *J. Phys. Chem. C* **2016**, *120*, 14575.

[28] P. Y. Zhao, H. X. Wang, L. W. Wu, L. L. Chen, Z. M. Cai, L. T. Li, X. H. Wang, *Adv. Energy Mater.* **2019**, *9*, 1803048.

[29] J. L. Li, F. Li, Z. Xu, S. J. Zhang, *Adv. Mater.* **2018**, *30*, 1802155.

[30] P. S. V. Mocherla, C. Karthik, R. Ubic, M. S. Ramachandra Rao, C. Sudakar, *Appl. Phys. Lett.* **2013**, *103*, 022910.

[31] X. D. Qi, J. Dho, R. Tomov, M. G. Blamire, J. L. MacManus-Driscoll, *Appl. Phys. Lett.* **2005**, *86*, 062903.

[32] A. Zeb, S. J. Milne, *J. Eur. Ceram. Soc.* **2014**, *34*, 3159.

[33] V. Westphal, W. Kleemann, M. D. Glinchuk, *Phys. Rev. Lett.* **1992**, *68*, 847.

[34] M. D. Glinchuk, R. Farhi, *J. Phys.: Condens. Matter* **1996**, *8*, 6985.

[35] R. Pirc, R. Blinc, *Phys. Rev. B* **1999**, *60*, 13470.

[36] A. A. Bokov, Z. G. Ye, *J. Mater. Sci.* **2006**, *41*, 31.

[37] X. H. Liu, Y. Li, X. H. Hao, *J. Mater. Chem. A* **2019**, *7*, 11858.

[38] N. N. Luo, K. Han, F. P. Zhuo, C. Xu, G. Z. Zhang, L. J. Liu, X. Y. Chen, C. Z. Hu, H. F. Zhou, Y. Z. Wei, *J. Mater. Chem. A* **2019**, *7*, 14118.

[39] Z. Kutnjak, B. Vodopivec, R. Blinc, *Phys. Rev. B* **2008**, *77*, 054102.

[40] D. S. Fu, H. Taniguchi, M. Itoh, S. Koshihara, N. Yamamoto, S. Mori, *Phys. Rev. Lett.* **2009**, *103*, 207601.

[41] H. R. Jo, C. S. Lynch, *J. Appl. Phys.* **2016**, *119*, 024104.

[42] Z. B. Pan, L. M. Yao, J. W. Zhai, H. T. Wang, B. Shen, *ACS Appl. Mater. Interfaces* **2017**, *9*, 14337.

[43] S. V. Matrenin, B. S. Zenin, R. V. Tayukin, *IOP Conf. Ser.: Mater. Sci. Eng.* **2015**, *93*, 012040.

[44] K. Maca, V. Pouchlý, K. Bodišová, D. Galusek, *J. Eur. Ceram. Soc.* **2014**, *34*, 4363.

[45] R. Waser, *Ferroelectrics* **1992**, *133*, 109.

[46] K. J. Laidler, *J. Chem. Educ.* **1984**, *61*, 494.

[47] W. Weibull, *J. Appl. Mech.* **1951**, *18*, 293.

[48] A. M. Glazer, *Acta Crystallogr. A* **1975**, *31*, 756.

[49] I. Calisir, D. A. Hall, *J. Mater. Chem. C* **2018**, *6*, 134.

[50] I. Levin, V. Krayzman, M. G. Tucker, J. C. Woicik, *Appl. Phys. Lett.* **2014**, *104*, 242913.

[51] Y. Yoneda, Y. Kitanaka, Y. Noguchi, M. Miyayama, *Phys. Rev. B* **2012**, *86*, 184112.

[52] Z. Y. Liu, H. Q. Fan, M. M. Li, *J. Mater. Chem. C* **2015**, *3*, 5851.